Supplementary Note 1: Determining experimental parameters from the anisotropic difference scattering

The anisotropic XDS (S_2) signal was used to determine the t_0 and σ_{IRF} of the experiment. With octahedral symmetry, the structural dynamics of $[Fe(bpy)_3]^{2+}$ are not expected to contribute to the anisotropic difference scattering signal. The S_2 signal should thus arise predominantly from Nuclear-Coordinate Impulse-Response (NCIR) of water, induced by stimulated Raman processes of the pump laser.[1] The S_2 signal is shown in Figures S1A, and is well described its first two singular vectors, which are shown in Figure S1B. The description of the data provided by the first two singular vectors at selected time delays are shown in Figure S1C, and their summed amplitude is taken as the impulsive nuclear x-ray scattering (INXS) signal (Figure S1D, blue dots). The INXS signal is modeled directly by the NCIR signal which has been independently determined through optical heterodyne-detected optical Kerr-effect (OHD-OKE) experiments.[1] This reference NCIR signal, red curve of Figure S1D, is fitted to the INXS signal by convoluting it by a Gaussian describing the t_0 and σ_{IRF} of the x-ray experiment together with a small constant signal growing in with the same Gaussian. The best description (smallest χ^2) of the INXS signal, is obtained by convoluting the NCIR signal with a Gaussian centered at -65 ± 10 fs with a width of 64 ± 16 fs (FWHM), and is shown as the yellow curve of Figure S1D. The determination of the two parameters is almost uncorrelated as illustrated by the correlation plot shown in Figure S1E. The time-axis of all other transients has been shifted by the identified -65 fs such that time-zero t_0= 0 ± 10 fs. Since the NCIR signal of water is peaking already at 20 fs time delay,[1] it grows in significantly faster than either the XES or the isotropic XDS signals (which are dominated by structural and electronic dynamics of $[Fe(bpy)_3]^{2+}$ respectively). The INXS signal therefore provides the most accurate means of determining the σ_{IRF} and t_0.

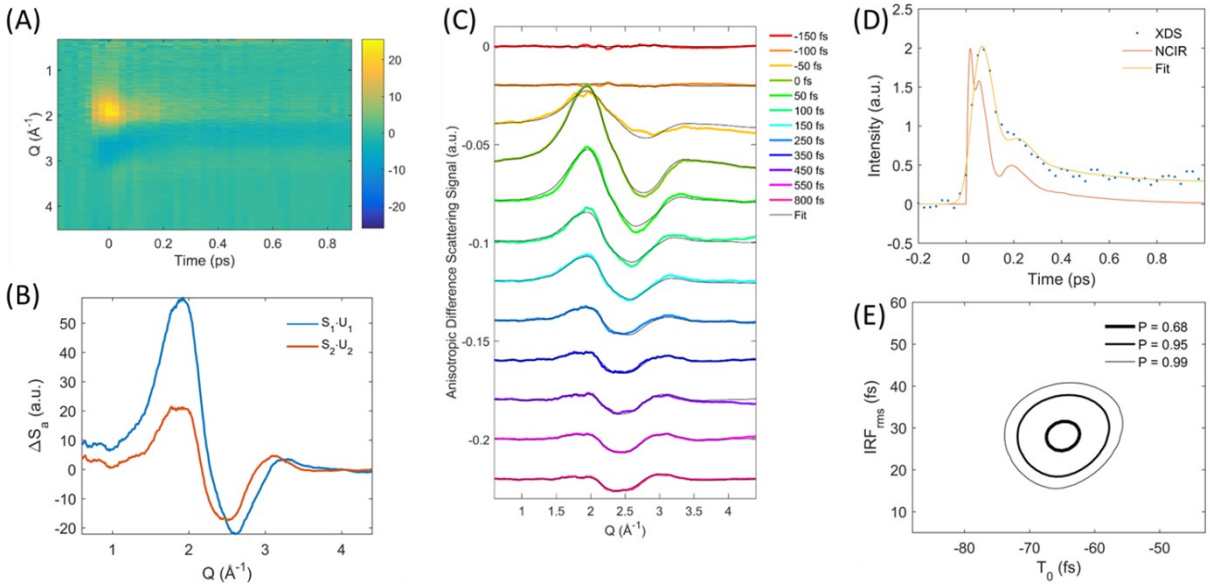

Figure S1. Determining experimental parameters from the anisotropic difference scattering. Singular value decomposition of the anisotropic (S_2) difference scattering signal (A) is dominated by the first two singular vectors (B). The data is well described by these two components as illustrated for selected time delays in (C). The amplitude of the anisotropic signal is given by the sum of the contribution from these two singular vectors, and shown as blue dots in (D). The dynamics of the amplitude of the S_2 signal is well described by the optically determined nuclear-coordinate impulse-response (red), convoluted by a Gaussian centered at -65 ± 10 fs with a width of 27 ± 7 fs (rms) (yellow). The correlation between center and width of the Gaussian convolution is shown in (E).

Supplementary Note 2: Dynamics of the parameters determined from XDS

The evolution of the parameters fitted to the XDS data recorded for $[Fe(bpy)_3]^{2+}$ are shown in Figure S2. Note that the XDS data includes data between 800 fs and 1.5 ps which were measured in a separate series of scans with lower time resolution (IRF = 85 fs FWHM), and appended to the high resolution -200 to 800 fs data.

The time dependent Fe-N bond length dynamics shown in Figure S2A, display clear oscillations for $t < 1$ ps. The average excited state Fe-N distance undergoes a 15% decrease throughout the full 1.5 ps time window following the initial expansion. This shortening of the average excited state Fe-N bond length follows from the anharmonic potential energy surface of the ^{5}MC state, which is shallower towards longer Fe-N distances, meaning that vibrational cooling of the highly excited Fe-N symmetric stretching vibration leads to a contraction of the average Fe-N bond length. The dephasing of the oscillations is significantly faster than the vibrational cooling, with the loss of coherence preceding vibrational cooling. We have quantified the time scales of the Fe-N bond length dynamics by fitting the 250 fs – 800 fs time range with a damped sinusoid overlaid with an exponential decay (blue curve of Figure 4F) retrieving the frequency and dephasing lifetime of the oscillations. We have fitted the > 600 fs Fe-N bond length shortening and corresponding decrease in cage signal by a single-exponential decay towards the previously reported excited state Fe-N bond length distance and cage response amplitude.[2, 3] We retrieve a period for the Fe-N oscillations of 235 ± 14 fs matching the 236 fs Fe-N stretch oscillation observed in both TA and XANES experiments,[4, 5] a dephasing lifetime of 340 ± 80 fs matching the XANES experiments,[5] and we retrieve a lifetime for the vibrational cooling of 1.4 ± 0.3 ps, fitted for both Fe-N distance and cage response, similar to the 1.6 ± 0.1 ps lifetime of vibrational cooling retrieved from the XANES experiments.[5]

The time dependent cage signal amplitude is shown in Figure S2B. As discussed in reference,[6] this component is calculated from pairwise RDF's with one atom in the solute and one in the solvent. Thus, this term arises from changes in the distance between the solute and the solvent molecules. For $[Fe(bpy)_3]^{2+}$ undergoing spin-crossover in aqueous solution,[7, 8] the changes in the first solvation shell is dominated by oxygen atoms of water molecules in the innermost solvation shell moving closer to the Fe-center (see e.g. Figure 4 of ref. [8]). The approach of the oxygen atoms to the iron center provides the largest solute-solvent pair correlation in the simulated cage signal (Figure 4C) as seen by the strong positive difference signal at low Q which signifies a shortening of average distances (see SI for van Driel *et al.* for a detailed discussion).[9] The short-ranged nature of the difference scattering component is reflected in the time evolution seen in Figure S2B, where a pronounced oscillatory pattern with the same period as the Fe-N oscillation is evident. Following the onset and initial oscillations, the average cage signal also decrease by around 15% within the first 1.5 ps, in parallel to the Fe-N distance. The similarity of the cage and molecular structural signals shows that the solvation dynamics are very efficiently driven by the structural dynamics of the solute.

The time evolution of the magnitude of the changes in the bulk solvent structure due to deposition of thermal energy is shown in Figure S2C. In the present case this increase tracks the vibrational energy transfer from the solute to the solvent with an onset coinciding with the first outer turning point of the Fe-N oscillation, followed by a grow-in on several time scales, one approximately 0.8 ps and one somewhat longer. We interpret the first time scale as arising from impulsive energy deposition due to the fast stretching of the Fe-N bond leading to a collision with the nearest solvent molecules, and with the longer time scale arising from incoherent vibrational cooling of the solute molecules as energy is re-distributed on internal and external degrees of freedom. For the present data, this second process is however not fully quantifiable as the second grow-in is hard to track with a final value outside the time window measured in these experiments

The time evolution of the solvent density change is shown in Figure S2D. This term arises from changes in the average distance between solvent molecules and has most often been included in the analysis of data acquired on much longer time scales, ns to μs, where hydrodynamic expansion of the solvent sets in following impulsive energy deposition.[10, 11] However, in our previous work on $[Fe(bpy)_3]^{2+}$ including this term on also sub-ns time scales where there is no time for bulk expansion was observed to improve the model fit significantly. This was interpreted in the light of the simulations presented by Daku and Hauser[7] where an expulsion of two water molecules from the solvation cage into the bulk liquid was predicted. In agreement with previous observations,[3] the density undergoes a very fast grow-in, which we here can determine to be ~100 fs, followed by oscillations. These observations are inconsistent with the proposed model of solvent-shell reorganization leading to an increase in bulk-solvent density. We further note that the simulation study in ref. [7] has very recently been re-done with more advanced methods and improved statistics,[8] and the result of this newer study also brings the solvent-expulsion model into question. On this background we interpret the solvent-density term as arising from a solvation-cage re-ordering that gives rise to a change in scattering approximating that of a density increase.

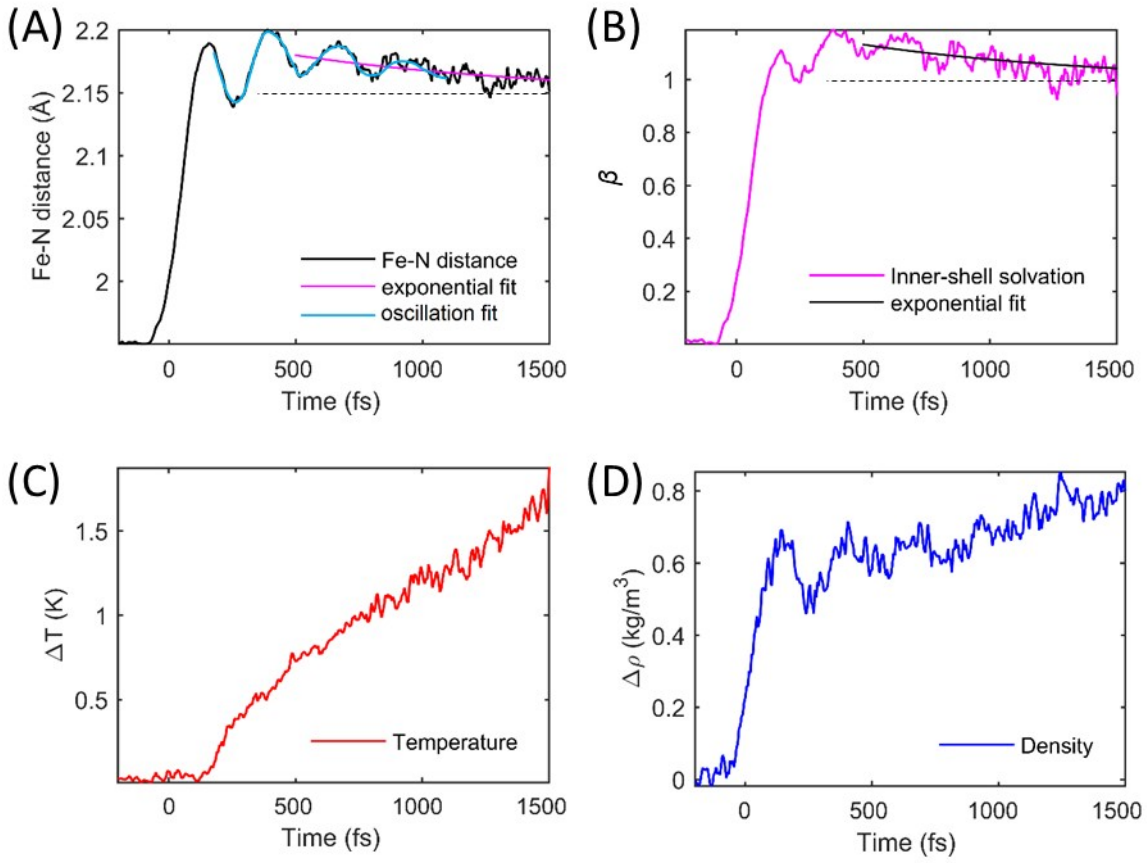

Figure S2. Time evolution of the four parameters determined from XDS. Dashed black lines in panel (A) and (B) shows the Fe-N bond length increase and cage response amplitude determined at >10 ps time delay.

Supplementary Note 3: Fitting the extracted electronic kinetics with an exponential model

Extracting the excited state kinetics without imposing an exponential decay of the MLCT state leads to the excited electronic state dynamics presented in Figure S3 (colored circles). The dynamics are qualitatively

similar to the ones extracted with exponentially constrained MLCT decay (see e.g. Figure 3C), note in particular the negative 'kink' in the ^{5}MC population at 300 fs time delay. Fitting the MLCT decay dynamics extracted without constrains (red line figure S3) returns the same 110 ± 8 fs MLCT lifetime as found when imposing the exponential decay already in the extraction of the excited state dynamics.

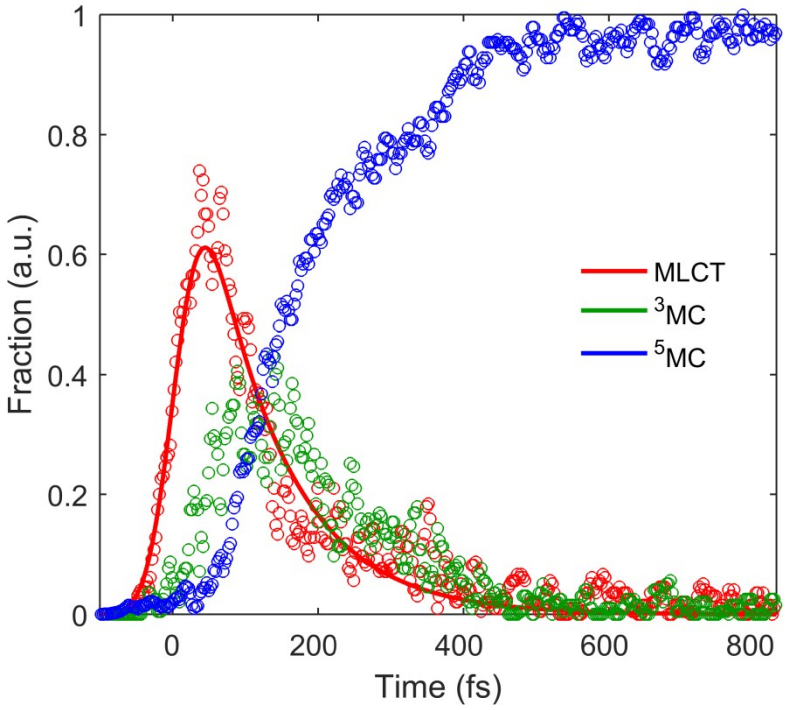

Figure S3. The electronic kinetics extracted from the XES without imposing an exponential decay of the MLCT state, together with an exponential fit of the MLCT decay dynamics.

Supplementary Note 4: Fitting the extracted electronic kinetics with an exponential model

Applying the model of Zhang et al. to the extracted electronic kinetics returns a 70 ± 8 fs ^{3}MC lifetime, well within the error reported by Zhang et al (see Figure S4).[12]

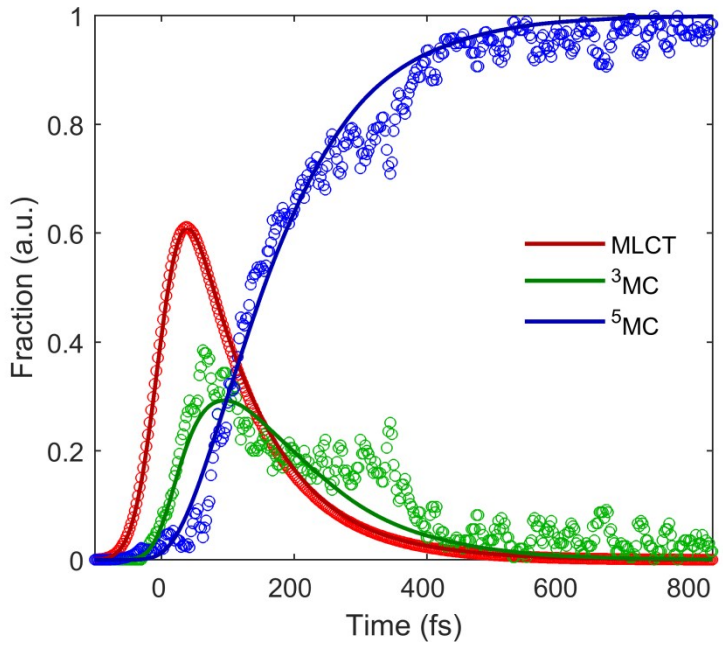

Figure S4. The electronic kinetics extracted from the XES as presented in Figure 3C, fitted by the model used by Zhang et al.[12]

Supplementary Note 5: Kinetics of the Fe Kβ XES data

The extracted excited state electronic dynamics extracted from the XES measurements shows a clear non-exponential feature at around 300 fs, most visible in the ^{5}MC population grow-in. This ~300 fs feature deviating from exponential-type dynamics is visible already in the kinetics of the raw difference signal illustrated in Figure S5A (colored circles). Figure S5A shows the kinetics of the XES signal at four different energies corresponding to the colored arrows of Figure S5B. The ~300 fs feature is most clearly pronounced in the 7054 eV shoulder dynamics, corresponding to the spectral range where the difference between ^{3}MC and ^{5}MC reference difference spectra is largest.

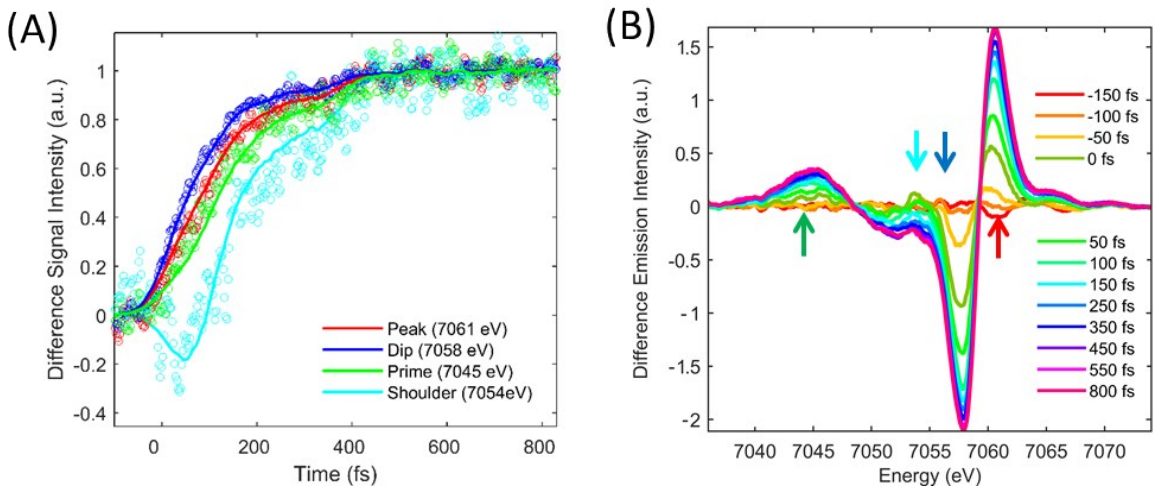

Figure S5. XES difference signal. (A) Kinetics of the difference data at four different energies (circles) and the description of the data provided by the extraction with model spectra (full curves). (B) Difference spectra at selected time delays, arrow indicates the energy of the presented dynamics.

Supplementary Note 6: Spectral deconvolution of the Fe Kβ XES data

Misalignment of one of the four analyzer crystals of the multicrystal spectrometer during the LCLS experiment resulted in distorted Kβ XES spectra. In order to remove this distortion the spectra were corrected with a following formula

$$S_{corr} = FT^{-1}\left\{\frac{FT\{D^*\}FT\{S_{uncorr}\}}{FT\{D^*\}FT\{D\}}\right\}$$

S_{corr} is the corrected spectrum, S_{uncorr} is uncorrected (measured) spectrum and D is the function describing the distortion defined by two delta peaks whose relative height and position correspond to misalignment of the fourth crystal. Figure S6 shows an example of a measured and a corrected spectra. Note that direct application of the deconvolution theorem would result in singularities and therefore before the division is carried out both numerator and denominator are multiplied by $FT\{D^*\}$. The correction procedure includes finding the suitable relative height and shift of the two delta peaks in D. We found that the most robust implementation of the deconvolution was reached when the deconvolved spectra were found by iteratively optimizing a numerically convolved trial spectrum against the measured data.

We initially sought to verify the assumption that a misalignment of a dispersive crystal in the von Hamos spectrometer was impacting the measured spectra ($S_{measured}$) by determining the distortion spectrum (D). D was determined by numerically convoluting a reference $[Fe(bpy)_3]^{2+}$ ground state spectrum (S_{ref}) with a trial distortion spectrum (D_T) to simulate a distorted $[Fe(bpy)_3]^{2+}$ ground state spectrum (S_D) matching $S_{measured}$. The relative height and relative distance between the two delta peaks in D_T were iteratively optimized such that χ^2 between $S_{measured}$ and S_D was minimized. We found that the optimized D consisted of two delta peaks of internal heights 0.23/0.77 and an energy difference of 4.32 eV (see Figure S7). The relative intensity between the two peaks is very close to the expected 0.25/0.75 distribution expected for one of the four von Hamos crystals being misaligned.

The corrected difference spectrum at each time delay was calculated using the optimized distortion spectrum. We found that the most robust deconvolution was achieved when implementing the deconvolution as an iterative numerical optimization of a trial deconvolution spectrum S_T. For each difference spectrum measured (S_{uncorr}), an initial S_T was taken as the spectrum itself. Numerical convolution of S_T with D, provided a deconvoluted trial spectrum S_{TD}, which was directly compared to S_{uncorr} providing a χ^2. S_T was then optimized by minimizing χ^2 between S_{uncorr} and S_{TD} in a Monte-Carlo like approach by adding a small (positive or negative) random value to each data point of S_T, convoluting it with D and assessing the change in χ^2 between S_{TD} and S_{uncorr}. Robustness was significantly improved by enforcing a 3-pt running median filter on S_T, which constitutes the only smoothing of the spectra shown in Figure 3A. The corrected

difference spectrum (S_{corr}) of each time delay can then be defined as the converged trial spectrum S_T. Simulated annealing and Monte-Carlo methods converged on indistinguishable S_T.

The result of the deconvolution process is illustrated in Figure S6.

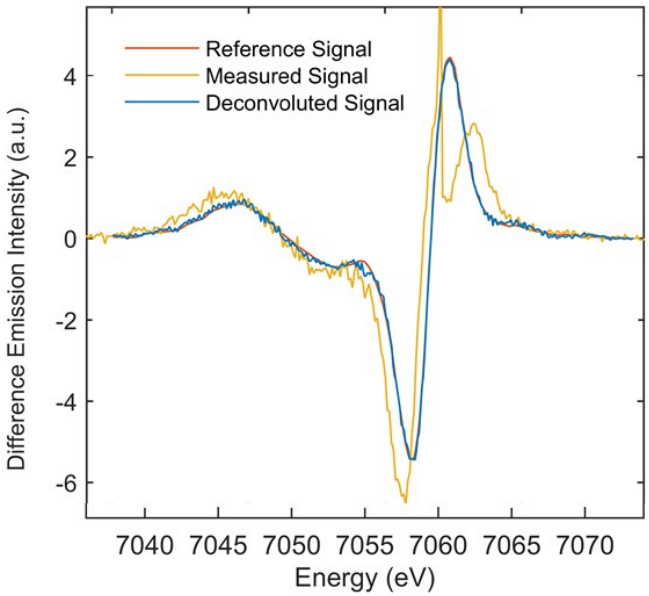

Figure S6. Spectral deconvolution of the Fe Kβ XES data. The reference difference signal for the ^{5}MC state (red), the measured difference signal at 800 fs (yellow) and the same 800 fs signal after the deconvolution process (blue).

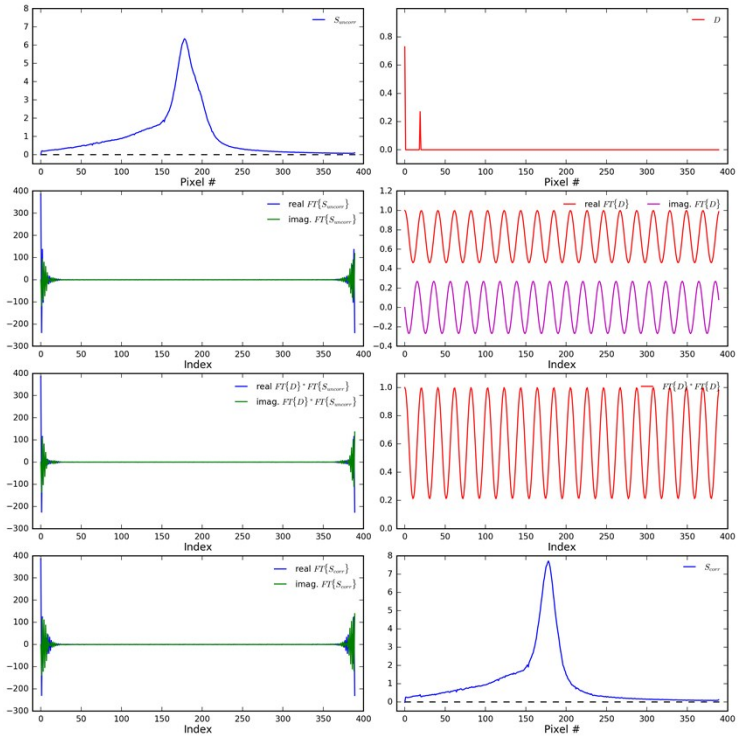

Figure S7. Correction of spectral distortion due to misalignment of one of the spectrometer crystals. Two delta peaks in D are shifted by 20 pixels (corresponding to 4.32 eV) and their relative heights are 0.77/0.23.

Supplementary Note 7: Extracting the Fe-N distance without a density contribution to the fit

With the open questions about the validity of the density contribution to the difference scattering signal at early time scales, we conducted a full analysis where the density contribution in the XDS fitting was explicitly set to 0 at all time delays. Figure S8A shows the fit at 150 fs time delay without including a density term in the fit, and can be directly compared to Figure 4F of the main text, showing that the residual from the fit increases when the density term is excluded. Figure 7SB shows the time-dependent Fe-N distance as a function of time, with and without a density term in the XDS fitting, illustrating that the Fe-N bond length change systematically increases by ≤0.01 Å for fits without at density term.

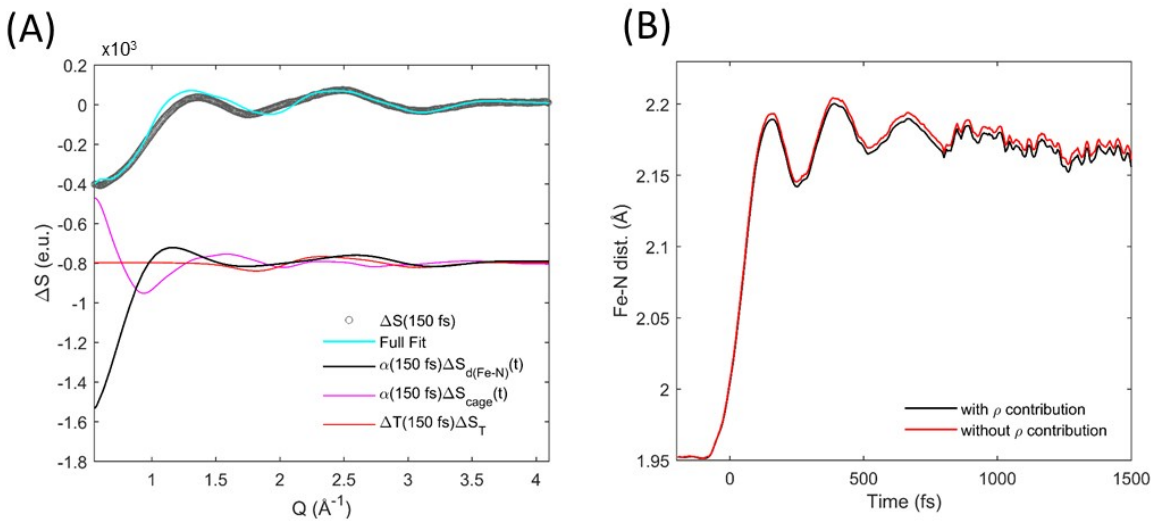

Figure S8. Extracting the excited state structural dynamics from XDS measurements without a density term. (A) Data, fit and fit components for the 150 fs time-delay. (B) Excited state Fe-N bond length distance extracted from XDS using the method described in the main text (black), and for a similar approach without including a density term in the analysis (red).

Supplementary Note 8: Kinetic model for extracting potential energy surfaces

The modelling of the excited state cascade of $[Fe(bpy)_3]^{2+}$ is simulated for 10^5 systems using an expansion of the model presented by Lemke *et al*.[5] The simulation takes the Fe-N bond length distance (x), the velocity with which it is changing (v), and the potential energy surface (S) for each system, and propagate them classically in time steps (Δt) of 1 fs, according to the equations of motion described in the following:

The velocity of particle n at time step t+1, $v_{n,t+1}$ is calculated from the velocity at time t, $v_{n,t}$ and the slope of the potential energy surface at which particle n is residing $S_{n,t}(x_{n,t})$ at its current position $x_{n,t}$:

$$v_{n,t+1} = v_{n,t} + S_{n,t}(x_{n,t}) \cdot \Delta t$$

To account for dephasing and damping, energy redistribution events, each system will transfer part of its kinetic energy to a thermal bath and cause a phase loss by inverting the momentum with a time constant of 400 fs. In line with the model of Lemke et al[13], upon a momentum inverting event, the system loses 60% energy to its surroundings, concurrent with a (normally distributed) stochastic change of velocity, coupling the system to a thermal bath. The thermal bath keeps the bond length distribution in line with the calculations of Daku and Hauser.[7]

$$v_{n,t+1}\begin{cases} -\sqrt{0.4}\cdot v_{n,t+1} + \sqrt{\gamma K_B T}\cdot l & r \le 1 - exp\left(-\frac{\Delta t}{400fs}\right) \\ v_{n,t+1} & \end{cases}$$

Where γ is a coupling parameter, K_B is the Boltzmann constant and T is the (absolute) temperature, and l is a normally distributed random number such that $-1 \le l \le 1$. Finally r is a random number such that $0 \le r \le 1$. Having updated the velocity, the Fe-N bond length distance of the system can be updated.

$$x_{n,t+1} = x_{n,t} + v_{n,t+1} \cdot \Delta t$$

Finally, the excited state potential energy surface occupied by each system is evaluated as follows:

$$S_{n,t+1}\begin{cases} P^{MLCT} & S_{n,t} = P^{MLCT}, T^{MLCT\rightarrow {}^3MC}_{n,t+1} = 0 \\ P^{{}^3MC}\begin{cases} S_{n,t} = P^{MLCT}, T^{MLCT\rightarrow {}^3MC}_{n,t+1} = 1 \\ S_{n,t} = P^{{}^3MC}, T^{{}^3MC\rightarrow {}^5MC}_{n,t+1} = 0 \\ S_{n,t} = P^{{}^5MC}, T^{{}^5MC\rightarrow {}^3MC}_{n,t+1} = 1 \end{cases} \\ P^{{}^3MC}\begin{cases} S_{n,t} = P^{{}^3MC}, T^{{}^3MC\rightarrow {}^5MC}_{n,t+1} = 1 \\ S_{n,t} = P^{{}^5MC}, T^{{}^5MC\rightarrow {}^3MC}_{n,t+1} = 0 \end{cases} \end{cases}$$

Where T designates whether the system is transitioning between excited states as follows.

$$T^{MLCT\rightarrow {}^3MC}_{n,t+1}\begin{cases} 1 & r \le 1 - exp\left(-\frac{\Delta t}{110fs}\right) \\ 0 & \end{cases}$$

$$T^{{}^3MC\rightarrow {}^5MC}_{n,t+1}\begin{cases} 1 & x_{n,t} < i^{{}^3MC/{}^5MC} \le x_{n,t+1} \ , \quad r \le p^{{}^3MC\rightarrow {}^5MC} \\ 0 & \end{cases}$$

$$T^{5_{MC\rightarrow}{}^{3}MC}_{n,t+1}\begin{cases}1 & x_{n,t+1} < i^{3_{MC}/{}^{5}MC} \leq x_{n,t} \quad , \quad r \leq p^{5_{MC\rightarrow}{}^{3}MC} \\ 0 & \end{cases}$$

With *r* being a random number such that $0 \leq r \leq 1$, and *p* being the transition probabilities at the intersection between MC potential energy surfaces. After v,x, and S has been determined for t+1 for each system, the parameters are stored and the process is repeated. Thus, excited state (S) and Fe-N distance (x) are calculated for each system, for each 1 fs time step, until the experimental time window has been covered by the simulation. Hereafter the simulated excited state dynamics can be quantitatively compared to the experimental results as described in the main text.

Supplementary note 9: DFT and MD calculations

In this analysis, we use the molecular structures for the LS and the HS states calculated by Daku and Hauser.[7] These structure were modified by changing the Fe-N bond length (symmetrically) in steps of 0.001 Å (from 1.95 Å to 2.20 Å) and keeping the other bond length constant. These modified structures were used in the fit of the experimental data (Eq.4).

The LS and HS structures were introduced into classical MD simulations with 4171 water molecules (OPLS2005 force field with the TIP4P water model) and the trajectories were run at a constant temperature for 2ns, keeping the solute structure fixed. Radial distribution functions of the solute-solvent atoms pair were obtained from the MD simulations and used to calculate the cage scattering signal as described in Dohn *et al*.[6]

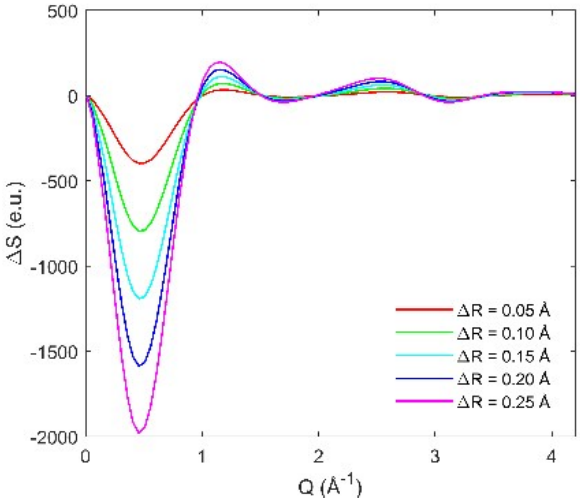

Figure S9. Difference scattering signal as a function of the Fe-N bond length change from the ground to the excited state of $[Fe(bpy)_3]^{2+}$.

Supplementary Note 10: Optical laser power dependence of the measurement

The fluence dependence of the optical response of $[Fe(bpy)_3]^{2+}$ has been published in the supporting information by the Zhang *et al*.[12] This shows the onset of saturation of the single photon absorption when pumping at 520 nm at roughly 100 $mJcm^{-2}$. The most detailed investigation of the fluence dependence at 400 nm can be found in the Thesis of Dr. Wojchiech Gawelda.[13] This work shows the appearance of a new spectral component to the transient absorption induced by excitation at 400 nm when using an 80 $mJcm^{-2}$ fluence that does not appear at low excitation fluence. The analysis of Gawelda indicates we could be observing a multiphoton source of difference signal at the 1-2% level, but we see no evidence of this signal in our measurement nor in prior measurements on $[Fe(bpy)_3]^{2+}$[5, 12] and the excitation levels used in the current publication are significantly lower than those used in many previous studies without seeing any significance difference in the comparable observables.[13-15]

References:

1. E. W. Castner, Y. J. Chang, Y. C. Chu and G. E. Walrafen, *J. Chem. Phys.*, 1995, 102, 653-659.
2. K. Haldrup, G. Vanko, W. Gawelda, A. Galler, G. Doumy, A. M. March, E. P. Kanter, A. Bordage, A. Dohn, T. B. van Driel, K. S. Kjaer, H. T. Lemke, S. E. Canton, J. Uhlig, V. Sundstrom, L. Young, S. H. Southworth, M. M. Nielsen and C. Bressler, *J. Phys. Chem. A*, 2012, 116, 9878-9887.
3. K. Haldrup, W. Gawelda, R. Abela, R. Alonso-Mori, U. Bergmann, A. Bordage, M. Cammarata, S. E. Canton, A. O. Dohn, T. B. van Driel, D. M. Fritz, A. Galler, P. Glatzel, T. Harlang, K. S. Kjaer, H. T. Lemke, K. B. Moller, Z. Nemeth, M. Papai, N. Sas, J. Uhlig, D. L. Zhu, G. Vanko, V. Sundstrom, M. M. Nielsen and C. Bressler, *J. Phys. Chem. B*, 2016, 120, 1158-1168.
4. G. Auböck and M. Chergui, *Nature Chem.*, 2015, 7, 629-633.
5. H. Lemke, K. S. Kjær, R. W. Hartsock, T. B. van Driel, M. Chollet, J. M. Glownia, S. H. Song, D. L. Zhu, E. Pace, S. F. Matar, M. M. Nielsen, M. Benfatto, K. J. Gaffney, E. Collet and M. Cammarata, *Nature Comm.*, 2017, 8, 15342.
6. A. O. Dohn, E. Biasin, K. Haldrup, M. M. Nielsen, N. E. Henriksen and K. B. Moller, *Journal of Physics B-Atomic Molecular and Optical Physics*, 2015, 48, 244010.
7. L. M. L. Daku and A. Hauser, *J. Phys. Chem. Lett.*, 2010, 1, 1830-1835.
8. L. M. L. Daku, *Phys. Chem. Chem. Phys.*, 2018, 20, 6236-6253.
9. T. B. van Driel, K. S. Kjær, R. W. Hartsock, A. O. Dohn, T. Harlang, M. Chollet, M. Christensen, W. Gawelda, N. E. Henriksen, J. G. Kim, K. Haldrup, K. H. Kim, H. Ihee, J. Kim, H. Lemke, Z. Sun, V. Sundström, W. Zhang, D. Zhu, K. B. Møller, M. M. Nielsen and K. J. Gaffney, *Nature Comm.*, 2016, 7, 13678.
10. K. S. Kjaer, T. B. van Driel, J. Kehres, K. Haldrup, D. Khakhulin, K. Bechgaard, M. Cammarata, M. Wulff, T. J. Sorensen and M. M. Nielsen, *Phys. Chem. Chem. Phys.*, 2013, 15, 15003-15016.
11. M. Cammarata, M. Lorenc, T. K. Kim, J. H. Lee, Q. Y. Kong, E. Pontecorvo, M. Lo Russo, G. Schiro, A. Cupane, M. Wulff and H. Ihee, *J. Chem. Phys.*, 2006, 124, 124504.
12. W. Zhang, R. Alonso-Mori, U. Bergmann, C. Bressler, M. Chollet, A. Galler, W. Gawelda, R. G. Hadt, R. W. Hartsock, T. Kroll, K. S. Kjaer, K. Kubicek, H. T. Lemke, H. W. Liang, D. A. Meyer, M. M. Nielsen, C. Purser, J. S. Robinson, E. I. Solomon, Z. Sun, D. Sokaras, T. B. van Driel, G. Vanko, T.-C. Weng, D. Zhu and K. J. Gaffney, *Nature*, 2014, 509, 345-348.
13. W. Gawelda, Doctor of Philosophy, Ecole Polytechnique Federale de Lausanne, 2006.
14. M. Khalil, M. A. Marcus, A. L. Smeigh, J. K. McCusker, H. H. W. Chong and R. W. Schoenlein, *J. Phys. Chem. A*, 2006, 110, 38-44.
15. C. Bressler, C. Milne, V. T. Pham, A. ElNahhas, R. M. van der Veen, W. Gawelda, S. Johnson, P. Beaud, D. Grolimund, M. Kaiser, C. N. Borca, G. Ingold, R. Abela and M. Chergui, *Science*, 2009, 323, 489-492.